Journal of Materials Chemistry A

ROYAL SOCIETY OF CHEMISTRY

PAPER

View Article Online
View Journal | View Issue

Check for updates

Cite this: *J. Mater. Chem. A*, 2024, **12**, 8205

Benzobisthiazole-substituted terpolymers for non-halogenated solvent-processed polymer solar cells with enhanced efficiency, thermal stability and mechanical robustness†

Soodeok Seo,‡[a] Hyesu Jeon,‡[a] Eun Sung Oh,[b] Jin-Woo Lee,[a] Chulhee Lim,[a] Trieu Hoang-Quan Nguyen,[a] Tan Ngoc-Lan Phan,[a] Dahyun Jeong,[a] Michael J. Lee,[c] Taek-Soo Kim[b] and Bumjoon J. Kim*[a]

High power conversion efficiency (PCE), eco-friendly processing, and long-term stability are essential for the commercialization of polymer solar cells (PSCs). In this study, we develop PM6-based terpolymer donors (PM6-DTzB*X*, where $X = 5–20$), by substituting the benzodithiophene-dione (BDD) unit with the benzobisthiazole (DTzB) unit, which aims to tune the crystalline properties of the polymers as well as achieving a blend morphology with sufficient intermixed domains. The DTzB-incorporating polymer donors (P_Ds) demonstrate stronger intermolecular interactions with a Y6-BO small molecule acceptor (SMA) and exhibit more pronounced crystalline properties than the reference PM6 P_D. Consequently, PM6-DTzB10 P_D-based PSCs achieve a higher PCE of 16.8% compared to that of PM6-based PSCs (15.6%) when processed in a non-halogenated *ortho*-xylene solvent. Furthermore, under thermal stress at 100 °C for 100 h, PM6-DTzB10-based PSCs maintain 88% of the initial PCE and exhibit enhanced thermal stability compared to PM6-based PSCs, which retain 72% of the initial PCE. Additionally, the PM6-DTzB10:Y6-BO blend films demonstrate a 7-fold increase in stretchability with a crack onset strain (COS) of 11.7%, compared to the PM6:Y6-BO blend films (COS = 1.7%). These enhancements in the PCE, thermal stability, and mechanical robustness can be mainly ascribed to the formation of a well-intermixed P_D:SMA blend morphology and enhanced crystalline properties of PM6-DTzB P_Ds. This study highlights the potential of the terpolymer strategy in developing efficient, thermally stable, and mechanically robust PSCs.

Received 6th January 2024
Accepted 21st February 2024

DOI: 10.1039/d4ta00117f

rsc.li/materials-a

1. Introduction

Polymer solar cells (PSCs) are gaining attention as a promising next-generation energy source due to their advantages including semi-transparency, and cost-effective large-area fabrication through solution processing.[1–4] Various polymer donors (P_Ds) and small-molecule acceptors (SMAs) have been developed to enhance the power conversion efficiency (PCE) of PSCs, with some achieving PCE values exceeding 19%.[5–13] However, the commercialization of PSCs necessitates the replacement of hazardous halogenated solvent-based processing, such as the use of chloroform and chlorobenzene, with more eco-compatible alternatives.[14–21] However, solution processing based on non-halogenated solvents results in PSCs with lower PCE values than those processed with halogenated solvents, mainly due to unoptimized P_D:SMA blend morphologies.

The unfavorable blend morphology primarily stems from the lower solubilities of P_Ds and SMAs and their unoptimized aggregated structures in non-halogenated solvents.[14,22,23] In particular, molecular incompatibility between the P_D and SMA often leads to severe phase separation between their respective domains during the film formation process. This unoptimized blend morphology adversely affects charge generation and transport in PSCs, resulting in decreased PCEs. In addition, an excessively phase-separated morphology is prone to degrade under external stresses such as light and heat, resulting in decreased photo, thermal, and mechanical stabilities of the PSCs.[24–27] Therefore, the design of active layer materials with sufficient solubilities in non-halogenated solvents and

[a]*Department of Chemical and Biomolecular Engineering, Korea Advanced Institute of Science and Technology (KAIST), Daejeon 34141, Republic of Korea. E-mail: bumjoonkim@kaist.ac.kr*

[b]*Department of Mechanical Engineering, Korea Advanced Institute of Science and Technology (KAIST), Daejeon 34141, Republic of Korea*

[c]*Department of Mechanical Engineering, College of Engineering, Kyung Hee University, Yongin 17104, Republic of Korea*

† Electronic supplementary information (ESI) available. See DOI: https://doi.org/10.1039/d4ta00117f

‡ These authors contributed equally to this work.

improved donor/acceptor interactions is imperative to simultaneously achieve both high performance and stability of the PSCs. For example, pairing donor and acceptor materials with improved molecular compatibility can prevent excessive separation between domains by reducing the thermodynamic penalty for formation of large donor–acceptor interfaces. The presence of sufficient donor–acceptor interfaces and intermixed domains can enhance the exciton dissociation and charge generation efficiency, resulting in higher short-circuit current density (J_{sc}), fill factor (FF), and PCE values in the PSCs.[28] Importantly, the P_D:SMA blend film with sufficient intermixed domains can prevent the occurrence of cracks at the P_D:SMA interfaces by effectively dissipating mechanical stress, and enhancing the mechanical robustness of the PSCs.[29–31]

The design of terpolymer-type P_Ds featuring D–A_1–D–A_2 type backbones has proven to be an effective strategy for enhancing the molecular compatibility of typical alternating-type P_Ds (D–A_1) with SMAs by replacing the A_1 block with a carefully selected A_2 block.[32–40] A suitable proportion of the A_2 block in the terpolymer-type P_D can effectively control its surface tension, which determines the enthalpic interaction with the SMA at the donor–acceptor interfaces. For instance, Cao *et al.* designed a random terpolymer-type P_D (JD40-BDD20) by adjusting the molar ratio of dithienobenzothiadiazole (TBT) and benzodithiophene-dione (BDD) units.[23] The use of the JD40-BDD20 terpolymer resulted in a reduced phase separation with the PJTVT acceptor compared to the control JD40 P_D due to its higher miscibility with the acceptor. As a result, the JD40-BDD20-based PSC demonstrated a higher PCE of 16.35% than that (14.05%) of the JD40-based PSC in *ortho*-xylene (*o*-xylene) processing. As another example, our group introduced ethyl thiophene-3-carboxylate units into the D18 P_D backbone to yield terpolymer-type P_Ds (PBET 10–50), which enabled a P_D:Y6-BO SMA blend morphology with sufficient intermixed domains compared to that with the reference D18.[33] PBET 10–50 enabled solution processing in *o*-xylene to construct a PSC with a PCE of 15.5%, whereas solution processing of D18 P_D was nearly impossible due to its very poor solubility in *o*-xylene. These studies suggest that developing terpolymer-type P_Ds can effectively increase their solubility in non-halogenated solvents and improve the molecular compatibility with SMAs. However, most random terpolymers inevitably exhibit reduced crystalline properties compared to alternating copolymers because random incorporation of the third A_2 unit into the P_D polymer results in the distortion of the molecular conformation and interferes with the effective formation of intermolecular assembly.[22,35] This decreased crystallinity of P_Ds can negatively influence the charge transport properties of the film, compromising the PCE values of the PSCs. Therefore, it is essential to design and incorporate an appropriate third unit into the P_D backbone that not only ensures higher crystalline and electrical properties but also maintains its sufficient processability in eco-friendly solvents.

In this study, we develop a new series of terpolymer-type P_Ds (PM6-DTzB*X*, $X = 5$, 10, and 20) by incorporating the benzo[1,2-*d*:4,5-*d*′]bis(thiazole) (DTzB) unit into the PM6 P_D backbone, replacing the BDD unit. Then, we utilize them to produce efficient and stable PSCs using non-halogenated solvent-based processing. We select the DTzB unit as the third component in the P_D for the following reasons: (1) the DTzB unit, containing nitrogen atoms, offers higher polarity and hydrophilicity than the BDD unit, thereby enhancing the molecular compatibility of the P_Ds with SMAs.[41–43] (2) The thiazole units in the DTzB block facilitate strong molecular interactions with adjacent thiophenes through a N–S noncovalent bonding.[44–47] This improved intra- and inter-molecular interaction can overcome the inherent limitations of random terpolymers, resulting in P_Ds with higher crystallinity and superior charge transport properties. As a result, with *o*-xylene solvent-based processing, PM6-DTzB10 P_D-based PSCs achieve a higher PCE of 16.8% compared to PM6-based PSCs (PCE = 15.6%). This increase is mainly attributed to higher crystallinity and hole mobility of the PM6-DTzB10. In addition, the PM6-DTzB10:SMA blend exhibits decreased domain size and purity compared to those of the reference PM6:SMA blend. This improved morphology of the PM6-DTzB10:SMA blend contributes to enhanced thermal stability and mechanical robustness through the formation of large donor–acceptor interfaces. Under continuous heating at 100 °C for 100 h, PM6-DTzB10-based PSCs maintain 88% of the initial PCE and exhibit enhanced thermal stability compared to PM6-based PSCs retaining 72% of the initial PCE. Moreover, the PM6-DTzB10:Y6-BO blend film exhibits remarkably enhanced stretchability with a higher crack onset strain (COS) value of 11.7%, compared to the PM6:Y6-BO blend film (COS = 1.7%). This study highlights the importance of selecting the third unit in terpolymer P_Ds to simultaneously enhance the P_D crystallinity and P_D–SMA interaction for achieving highly efficient and stable PSCs.

2. Results and discussion

2.1. Synthesis and characterization of materials

To explore the impact of the incorporated DTzB unit in the P_D chain on polymer properties and photovoltaic performance, PM6-DTzB*X* ($X = 5$, 10, and 20) terpolymers were synthesized. Here, *X* represents the molar fraction of the DTzB unit relative to the benzodithiophene (BDT) unit in the P_D backbone. The planar-structured DTzB unit was chosen to yield the PM6-DTzB*X* terpolymers for several reasons. (1) The nitrogen atoms in the DTzB unit can effectively enhance the polarity of the resulting polymers, reducing the thermodynamic immiscibility between the PM6-DTzB*X* terpolymers and SMAs.[41,48] (2) The thiazole units in the DTzB block promote strong N–S noncovalent bonding with thiophene, enhancing intra- and intermolecular interactions between P_Ds.[42] (3) Importantly, the DTzB unit has a fused ring structure without an alkyl solubilizing group, which helps to reinforce the backbone planarity of the PM6-DTzB*X* terpolymers.[49,50] These factors can synergistically improve the crystallinity of the P_D, thereby enhancing its charge-transporting capability.

Fig. 1a presents the chemical structures of the P_D and 2,2′-((2*Z*,2′*Z*)-((12,13-bis(2-butyloctyl)-3,9-diundecyl-12,13-dihydro-[1,2,5]thiadiazolo[3,4-*e*]thieno[2″,3″:4′,5′]thieno[2′,3′:4,5]pyrrolo[3,2-*g*]thieno[2′,3′:4,5]thieno[3,2-*b*]indole-2,10-diyl)

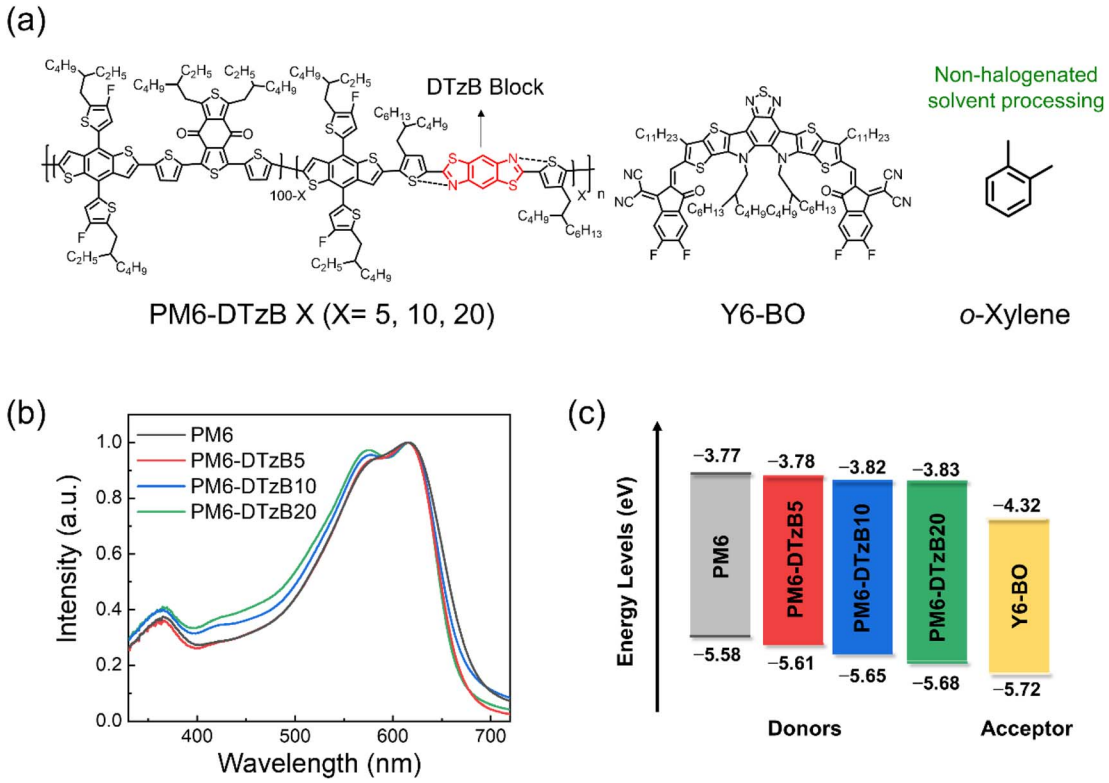

Fig. 1 (a) Chemical structures of the materials and a processing solvent used in this study. (b) UV-vis absorption spectra of P_D films. (c) Energy levels of the materials used in this study.

bis(methanylylidene))bis(5,6-difluoro-3-oxo-2,3-dihydro-1*H*-indene-2,1-diylidene))dimalononitrile (Y6-BO) SMA. Y6-BO was selected as a SMA due to its excellent light absorption ability, electron mobility, and sufficient solubility in processing solvents including *o*-xylene. The synthetic details of the DTzB monomer and P_Ds are provided in the Experimental section of the ESI (Fig. S1 and S2†). All P_Ds were synthesized to have similar number-average molecular weight (M_n) values ranging from 46 to 49 kg mol^{-1} (Table 1). We also confirmed that all P_Ds exhibited sufficient solubility in *o*-xylene (>40 mg mL^{-1}).

Ultraviolet-visible (UV-vis) absorption spectra of the P_Ds in film and solution are shown in Fig. 1b and S3,† respectively. Interestingly, with an increase in the quantity of DTzB units within the P_D backbone, P_Ds exhibited enhanced light absorption in a broad range spectrum, including wavelengths from 400 to 550 nm. While the maximum absorption wavelengths (λ_{max}^{film}s) of the P_Ds were similar in a range of 615–617 nm, the wavelengths at their absorption edges (λ_{max}^{edge}s) gradually blue-shifted with increasing DTzB content in the P_Ds. For example, the λ_{max}^{edge}s of PM6, PM6-DTzB5, PM6-DTzB10, and PM6-DTzB20 were 685, 678, 677, and 673 nm, respectively. As a result, the optical bandgap (E_g^{opt}) of the P_Ds gradually increased with increasing content of the DTzB units (Table 1). The frontier molecular orbital energy levels of the P_Ds were measured by cyclic voltammetry (Fig. 1c and S4†). Increasing the content of DTzB units gradually down-shifted the highest occupied molecular orbital (HOMO) energy levels of the P_Ds. For example, the HOMO energy levels of PM6, PM6-DTzB5, PM6-DTzB10, and PM6-DTzB20 were −5.58, −5.61, −5.65, and −5.68 eV, respectively. Energy levels, which were estimated from density functional theory (DFT) calculations performed at the B3LYP/6-31G(d,p) level, supported the energy level trend observed in CV measurements (Fig. S5†). For example,

Table 1 Properties of the materials used in this study

Material	$M_n(Đ)^a$ [kg mol^{-1}]	$\lambda_{max}^{film\,b}$ [nm]	ε_{max}^{film} [$\times 10^5$ cm^{-1}]	$\lambda_{film}^{edge\,b}$ [nm]	$E_g^{opt\,c}$ [eV]	$E_{HOMO}{}^d$ [eV]	$E_{LUMO}{}^e$ [eV]
PM6	48.8 (2.6)	615	0.64	685	1.81	−5.58	−3.77
PM6-DTzB5	46.0 (2.5)	615	0.63	678	1.83	−5.61	−3.78
PM6-DTzB10	47.8 (3.6)	617	0.65	677	1.83	−5.65	−3.82
PM6-DTzB20	45.9 (3.2)	617	0.62	673	1.84	−5.68	−3.83
Y6-BO	—	829	1.13	886	1.40	−5.72	−4.32

[a] Determined by gel permeation chromatography eluting in 1,2,4-trichlorobenzene relative to polystyrene standards. [b] Estimated from the UV-vis spectra of the thin film state spin-coated from the *o*-xylene solution. [c] Estimated from the absorption onsets in thin films spin-coated from the *o*-xylene solution using $E_g^{opt} = 1240/\lambda_{film}^{edge}$. [d] Calculated from the cyclic voltammetry spectra. [e] LUMO = HOMO + E_g^{opt}.

the BDT-DTzB structure possessed a lower HOMO energy level (−5.24 eV) compared to that of the BDT-BDD structure (HOMO = −5.15 eV) in the simulation.[41,44] In addition, the BDT-DTzB structure exhibited a larger bandgap value (E_g = 2.92 eV) than the BDT-BDD structure (2.71 eV). Therefore, the downshifted HOMO energy levels of the P_Ds are attributed to the strong electron-withdrawing properties of DTzB units and an increased bandgap of the polymers. The down-shifted HOMO energy levels of the P_Ds are advantageous in achieving high V_{oc} of the PSCs.

The aggregation properties of the P_Ds were investigated by measuring temperature-dependent UV-vis absorption spectra in *o*-xylene solution (Fig. S6†). The degree of aggregation was quantified by comparing the ratio of maximum intensity at 100 °C to that at 20 °C ($I_{max}^{100\ °C}/I_{max}^{20\ °C}$). PM6-DTzB P_Ds showed stronger aggregation ($I_{max}^{100\ °C}/I_{max}^{20\ °C}$ = 0.84–0.88) compared to PM6 P_D ($I_{max}^{100\ °C}/I_{max}^{20\ °C}$ = 0.77) (Table S1†). This result suggests that introducing the DTzB unit into the P_D backbone enhances the intermolecular interaction between P_D chains, leading to a higher degree of aggregation.[41]

The crystalline properties of neat P_D films were investigated using grazing incidence X-ray scattering (GIXS). In the GIXS 2D image and line-cut profiles, all P_Ds predominantly exhibited a face-on packing orientation, as evidenced by distinct (100) peaks in the in-plane (IP) direction and (010) peaks in the out-of-plane (OOP) direction (Fig. S7 and S8†).[51] For a quantitative comparison of the relative crystallinity of the P_Ds, their coherence length (L_c) values for the (010) scattering peaks in the OOP direction ($L_{c(010)}$) were estimated using Scherrer's equation (Table S2†).[52] Interestingly, P_Ds containing DTzB units exhibited higher $L_{c(010)}$ values (1.2 nm for PM6-DTzB10 and 1.3 nm for PM6-DTzB20) than PM6 ($L_{c(010)}$ = 0.6 nm), suggesting relatively larger crystal sizes in the film. The higher crystallinity of PM6-DTzB P_Ds compared to PM6 may be attributed to their stronger aggregation in solution, which helps forming well-ordered intermolecular assemblies during the film formation by solution processing.[53]

The charge transport abilities of P_D films were assessed by measuring the space charge limited current (SCLC) (Table S3†). The hole mobilities (μ_hs) of neat P_Ds gradually increased with increasing DTzB content. For example, the μ_hs of PM6, PM6-DTzB10, and PM6-DTzB20 were 1.36 × 10^{-4}, 1.63 × 10^{-4}, and 1.72 × 10^{-4} cm^2 V^{-1} s^{-1}, respectively. The enhanced electrical properties of the DTzB-containing P_Ds compared to PM6 correlate with their enhanced aggregation and crystalline properties. It is notable that, while most random terpolymer-type P_Ds exhibited reduced crystalline and electrical properties

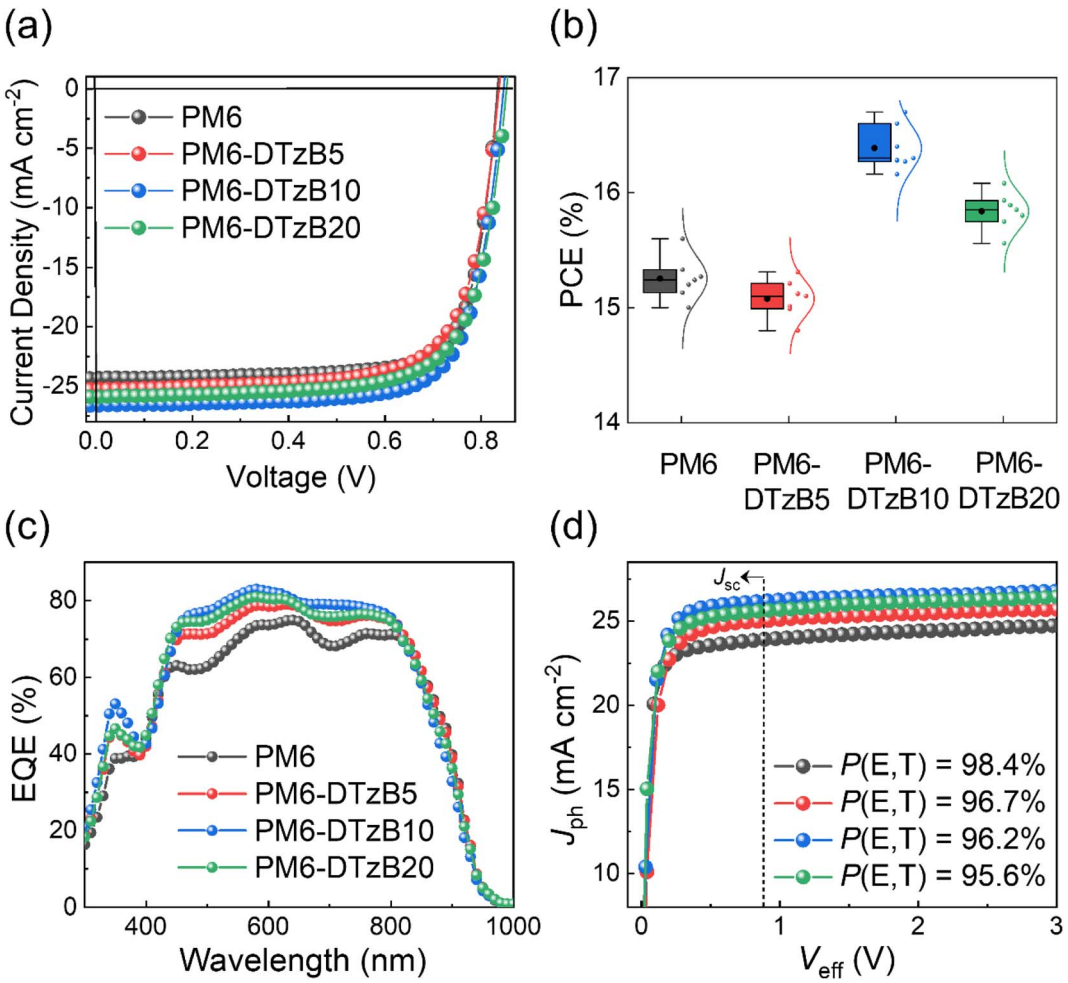

Fig. 2 (a) *J*–*V* curves, (b) PCE distributions, (c) EQE spectra, and (d) J_{ph}–V_{eff} curves of P_D:Y6-BO PSCs.

compared to the alternating copolymers owing to reduced structural regularity,[23,36,54] incorporation of the DTzB units does not compromise those properties.

2.2. Photovoltaic properties

The photovoltaic properties of all P_D:Y6-BO systems were investigated by fabricating conventional-type PSCs. The device architecture and fabrication procedure of PSCs are described in the Experimental section of the ESI.† All P_D:Y6-BO PSCs were processed in the *o*-xylene solvent. The current density–voltage (*J*–*V*) curves are shown in Fig. 2, and the corresponding photovoltaic parameters of the PSCs are presented in Table 2. Notably, the introduction of the DTzB unit instead of the BDD unit into PM6 P_D sequentially increased the open-circuit voltage (V_{oc}) of PSCs (0.830 V for PM6, 0.839 V for PM6-DTzB5, 0.842 V for PM6-DTzB10, and 0.856 V for PM6-DTzB20). This V_{oc} trend is correlated with the lower HOMO levels of DTzB-incorporating P_Ds than PM6 (Table 1). As a result, PM6-DTzB10-based PSCs exhibited a higher PCE (16.8%) than that of the control P_D (PM6, 15.6%), mainly owing to a higher V_{oc} value (0.842 V) and J_{sc} of 25.14 mA cm^{-2}, in comparison to PM6-based PSCs (J_{sc} = 24.03 mA cm^{-2}). However, a further increase in the content of DTzB units led to a decreased PCE value (16.1% for PM6-DTzB20:Y6-BO). The PCE distributions of PSCs fitted with Gaussian functions are displayed in Fig. 2b, indicating that all systems showed consistent PCEs. The external quantum efficiency (EQE) spectra of the PSCs are shown in Fig. 2c. The PM6-DTzB-based PSCs exhibited higher EQE responses in both the P_D absorption range (400–650 nm) and SMA absorption range (650–900 nm). This result supports higher J_{sc} values in DTzB-incorporating P_D:Y6-BO PSCs than PM6:Y6-BO PSCs. The calculated J_{sc} values matched well with the J_{sc}s measured from the PSCs with errors within 2% (Table 2).

To elucidate the origin of the different photovoltaic properties, we investigated the charge generation, dissociation, transport, and recombination behaviors of the P_D:Y6-BO blends. To investigate charge generation behaviors, the free charge carrier generation rate ($G(E,T)$) of the PSCs was evaluated. The $G(E,T)$ can be determined from the maximum exciton generation rate (G_{max}) and exciton dissociation probability ($P(E,T)$).[55] The calculation procedure of G_{max}, $P(E,T)$ and $G(E,T)$ is described in the Experimental section of the ESI.† The incorporation of an appropriate proportion of DTzB in P_Ds increased the J_{sat} and G_{max} of the blend film. For example, the G_{max} values of the PM6-DTzB5-, PM6-DTzB10-, and PM6-DTzB20-based blends were 1.89, 1.97 and 1.94 cm^{-3} s^{-1}, respectively, surpassing that of the PM6 based blend (1.81 cm^{-3} s^{-1}). Therefore, the $G(E,T)$ values of the PM6-DTzB-based blends were higher than that of the PM6-based blend (Fig. 2d and Table S4†). This result indicates that the incorporation of the DTzB unit in the P_D facilitates the charge generation and contributes to a higher J_{sc} during PSC operation.

The charge recombination properties of the PSCs were investigated by measuring their light intensity (P)-dependent J_{sc} and V_{oc} values (Fig. S9†).[56] All the blends exhibited similar slopes (α) in the logJ_{sc}–log P plots, indicating similar bimolecular recombination properties. The slope (S) in the V_{oc}–log P plots exhibited comparable values in PM6- (1.10 kT q^{-1}) and PM6-DTzB10-based PSCs (1.09 kT q^{-1}), indicating that the introduction of an appropriate amount of DTzB does not cause monomolecular/trap-assisted recombination.[57] The SCLC hole and electron mobilities of the P_D:Y6-BO blend films were measured to evaluate their charge transport abilities (Table S5†). All the blends showed similar μ_h values (2.1–2.3 × 10^{-4} cm^2 V^{-1} s^{-1}). Interestingly, the electron mobility (μ_e) was the highest in the PM6-DTzB10 blend (1.55 × 10^{-4} cm^2 V^{-1} s^{-1}) among all blends, resulting in the most balanced mobility ratio (μ_h/μ_e = 1.50) compared to other blends.[58]

2.3. Structural and morphological properties

The morphological properties of the P_D:Y6-BO blends were analyzed using GIXS, resonant soft X-ray scattering (RSoXS), and *in situ* UV-vis spectroscopy. We first measured the GIXS profiles of a neat Y6-BO film (Fig. S10 and S11†). Interestingly, the GIXS 2D image and line-cut profile of the Y6-BO neat film exhibited a much sharper and more distinct (010) peak along the OOP direction after annealing, which is attributed to its strong crystalline property. Subsequently, the GIXS profiles of the P_D:Y6-BO blend films were compared (Fig. 3a, b and S12†). All P_D:Y6-BO blend films displayed IP (100) and OOP (010) peaks around q_{xy} = 0.28–0.29 Å^{-1} and q_z = 1.45–1.95 Å^{-1}, respectively. Therefore, we assessed the relative degree of crystallinity (rDoC) of the (010) peaks of the P_D:Y6-BO blend films in the blend GIXS profiles (Fig. 3b and Table 3). The r-DoC$^{(010)}$ values increased in the following order: PM6:Y6-BO (0.65) < PM6-DTzB10:Y6-BO (0.87) < PM6-DTzB20:Y6-BO (1.00).[59]

To investigate the degree of phase separation between the P_D domain and Y6-BO domain, RSoXS measurements were performed, using a beam energy of 285.0 eV to maximize the contrast between the components in the blend films (Fig. 3c). The domain size and relative domain purity (r-DP) of the blends were estimated from their RSoXS profiles. Both the PM6:Y6-BO

Table 2 Photovoltaic performances of P_D:Y6-BO PSCs

P_D	V_{oc}[a] [V]	J_{sc}[a] [mA cm^{-2}]	Cal. J_{sc}[b] [mA cm^{-2}]	FF[a]	PCE$_{max\ (avg)}$[a] [%]
PM6	0.830	24.03	23.53	0.76	15.60 (15.13 ± 0.18)
PM6-DTzB5	0.839	24.59	24.33	0.73	15.37 (15.04 ± 0.21)
PM6-DTzB10	0.842	25.14	25.19	0.76	16.81 (16.14 ± 0.27)
PM6-DTzB20	0.856	25.02	24.65	0.74	16.08 (15.73 ± 0.18)

[a] Average values were obtained from 10 independent devices. [b] Calculated from EQE profiles.

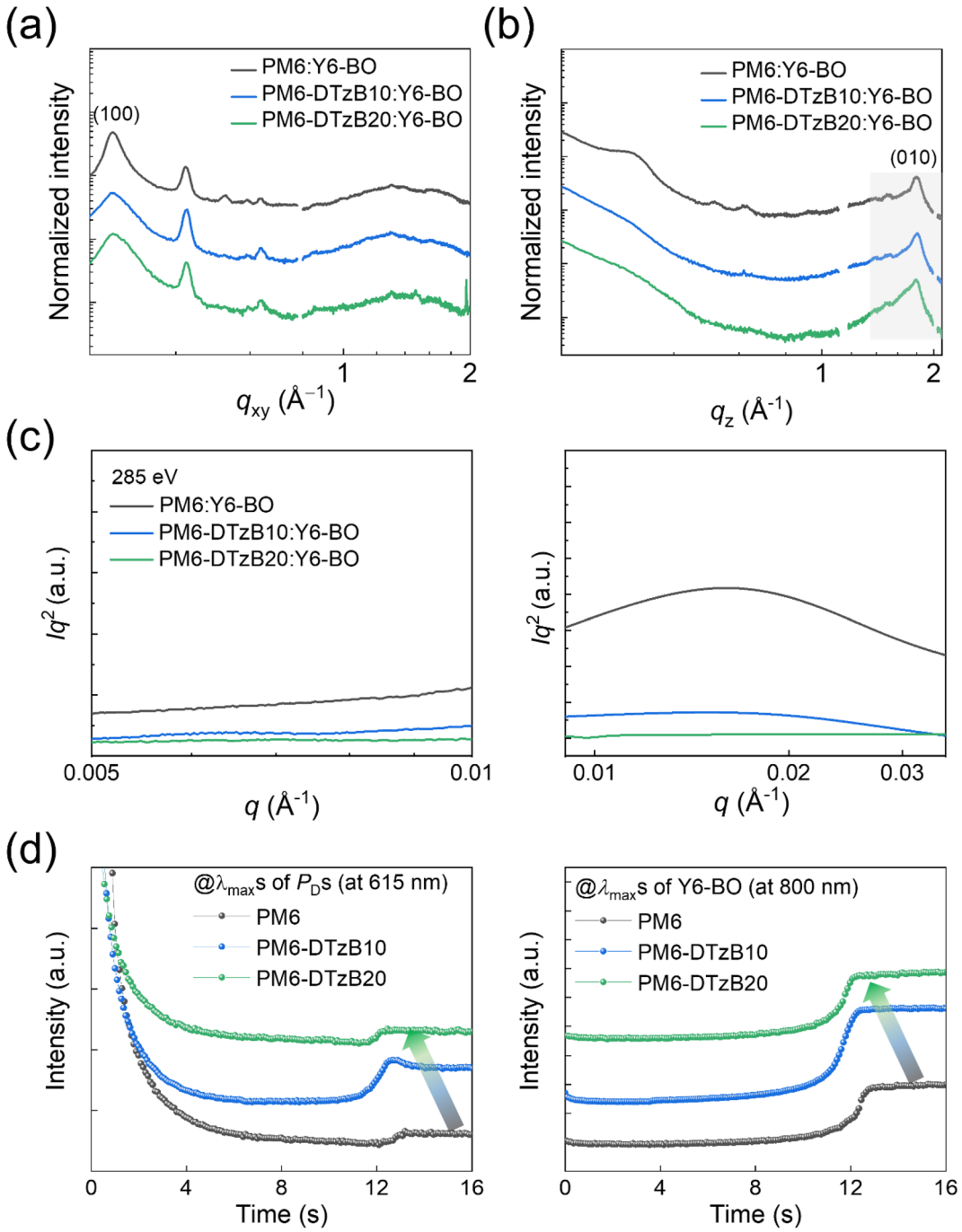

Fig. 3 GIXS line-cut profiles of P_D:Y6-BO blends in (a) the IP and (b) OOP directions. (c) RSoXS profiles of P_D:Y6-BO blends. (d) Time evolution of the UV-vis absorption intensity change of P_D:Y6-BO blends at 615 and 800 nm, respectively, during spin-coating.

blend (37.2 nm) and PM6-DTzB10:Y6-BO blend (33.1 nm) exhibited appropriate domain sizes for charge transport, while the PM6-DTzB20:Y6-BO blend showed no distinguishable peak. The *r*-DP was significantly higher for the PM6:Y6-BO blend (1.00) compared to the PM6-DTzB10-based blend (0.58) and PM6-DTzB20-based blend (0.50) (Table 3). A large interfacial area between donor and acceptor domains in a blend film is advantageous for charge generation and exciton dissociation. Therefore, the well-intermixed domain in the PM6-DTzB10:Y6-BO blend facilitates both higher J_{sc} and FF values compared to other blends.[60–63] At the same time, the incorporation of the DTzB unit into the PM6-DTzB P_Ds increased their crystalline properties, enhancing the charge transport properties and the PCE values in the PSCs. However, the PM6-DTzB20:Y6-BO blends exhibited an excessive amount of intermixed domains with lower domain size and purity, resulting in decreases of charge transport properties and photovoltaic performance.

The *in situ* UV-vis absorption measurements during the spin coating process were performed to investigate the film formation kinetics of different P_D:SMA blend systems and understand

Table 3 Morphological characteristics of P_D:Y6-BO blends

P_D	r-DOC$^{(010)a}$	Domain size^b [nm]	r-DP^b	t_{sat} at λ_{max} of P_D^{c} [s]	t_{sat} at λ_{max} of Y6-BO^c [s]
PM6	0.65	37.2	1	13.2	12.8
PM6-DTzB10	0.87	33.1	0.58	12.6	12.4
PM6-DTzB20	1	—	0.50	12.4	12.2

^{a} Estimated from the OOP (010) peak of GIXS line-cut profiles in the range of 1.45–1.95 Å^{-1}. ^{b} Estimated from the RSoXS profiles. ^{c} Estimated from the *in situ* UV-vis spectroscopy profiles of P_D:Y6-BO blends.

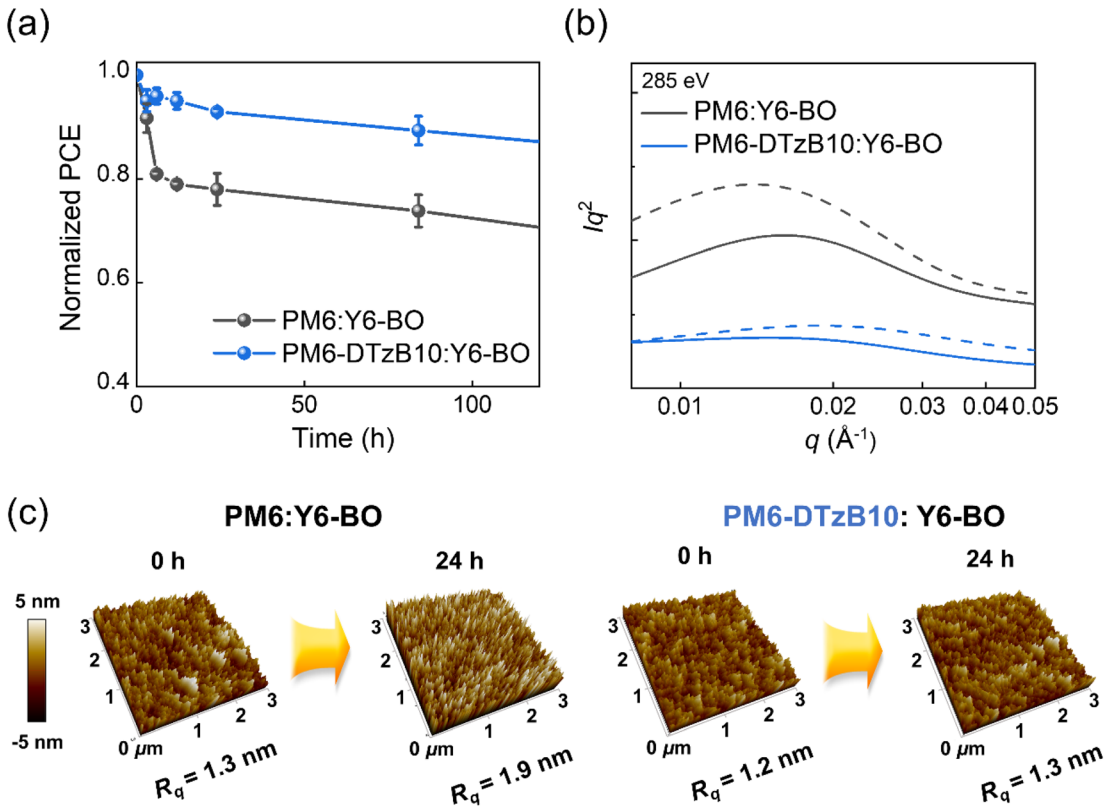

Fig. 4 (a) Thermal stability of P_D:Y6-BO PSCs under a 100 °C heating condition. (b) RSoXS profiles of the P_D:Y6-BO blend in the initial state (solid line) and after (dotted line) thermal annealing at 100 °C for 72 h. (c) AFM height images of P_D:Y6-BO blend films before (left) and after (right) thermal annealing at 100 °C for 24 h. Each image size is 3 μm × 3 μm.

its impact on the blend morphology (Fig. 3d, S13,† and Table 3). Extended quenching time in film solidification generally leads to a higher degree of liquid–liquid phase separation, typically resulting in more distinct phase separation between P_D and SMA domains.[64] The saturation times (t_{sat}s) in the absorption intensities at the maximum absorption wavelengths (λ_{max}) of P_Ds and Y6-BO were tracked. At the λ_{max} of P_Ds, t_{sat} values decreased in the following sequence: PM6 (13.2 s) > PM6-DTzB10 (12.6 s) > PM6-DTzB20 (12.4 s). These reduced t_{sat} values of PM6-DTzB P_Ds could be attributed to the stronger aggregation of PM6-DTzB P_Ds in *o*-xylene solvent compared to PM6, as shown in Fig. S6.† Similarly, the t_{sat} value of Y6-BO in the blend solution also followed a decreasing trend: PM6 (12.8 s) > PM6-DTzB10 (12.4 s) > PM6-DTzB20 (12.2 s). These results suggest that the incorporation of DTzB into the P_Ds accelerated the solidification of both the P_D and Y6-BO domains during film formation. This acceleration mitigates excessive phase separation and promotes the development of sufficiently intermixed domains.

To further investigate the changes in the molecular compatibility between the P_D and SMA depending on the terpolymer structure, we conducted contact angle measurements to estimate the interfacial tensions between the P_D and SMA (Fig. S14 and Table S6†).[65,66] The contact angles of water droplets on neat P_D films decreased in the order of PM6 (103.1°) > PM6-DTzB10 (100.9°) > PM6-DTzB20 (99.5°). Correspondingly, the surface tension values of P_Ds linearly increased from PM6 (19.2 mN m^{-1}) to PM6-DTzB10 (20.5 mN m^{-1}) and finally to PM6-DTzB20 (21.2 mN m^{-1}). These results are consistent with the previous studies where polymers containing DTzB units, such as PBB1 and PBB2 polymers, exhibited higher hydrophilicity than the reference polymers PM6 and PM7.[41,43] The surface tension value of the Y6-

BO SMA film was measured to be 24.8 mN m^{-1}. Thus, interfacial tension (γ^{D-A}) values between the P_D and Y6-BO decreased sequentially in the order of PM6:Y6-BO (0.79), PM6-DTzB10:Y6-BO (0.50), and PM6-DTzB20:Y6-BO blends (0.38). This result supports the view that the inclusion of DTzB units into the P_Ds reduces molecular incompatibility with the Y6-BO SMA, thereby thermodynamically facilitating the formation of larger donor–acceptor interfaces and intermixed domains.

2.4. Thermal stability

Next, to assess the influence of the polymer structure on the thermal stability of PSCs, the changes in the PCEs of both PM6- and PM6-DTzB10-based PSCs were monitored under continuous heating at 100 °C (Fig. 4a). The difference in PCE changes between the two blend systems was evident. This degradation was mainly attributed to the unstable initial morphology associated with the poor miscibility between the PM6 P_D and SMA.[67,68] PM6:Y6-BO-based PSCs showed a notable PCE decrease within 24 hours, maintaining less than 80% of their initial efficiency (PCE = 12.0%). In contrast, PM6-DTzB10:Y6-BO-based PSCs retained 93% of their initial PCE (PCE = 15.6%) under identical conditions.[33,69,70]

To elucidate the difference in thermal stability, morphological changes during the thermal annealing were compared through RSoXS and atomic force microscopy (AFM) measurements (Fig. 4 and Table S7†). RSoXS profiles revealed significant phase separation in the PM6:Y6-BO blend under thermal stress, with *r*-DP increasing from 0.65 to 1.00 (Fig. 4b). In contrast, the PM6-DTzB10:Y6-BO blend maintained a relatively consistent

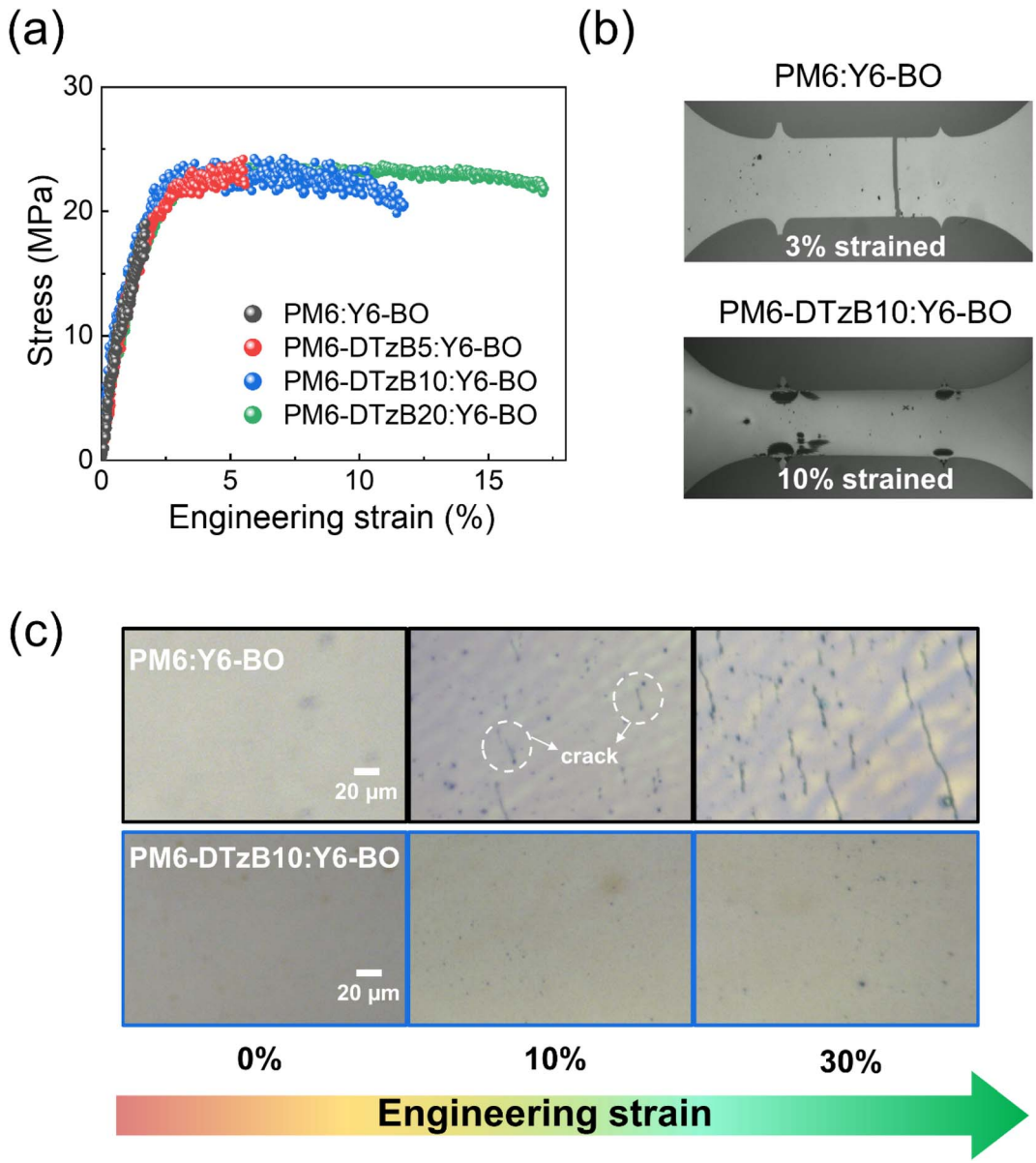

Fig. 5 (a) Stress–strain curves of P_D:Y6-BO blend films. Optical microscope (OM) images of the blend films (b) during the tensile test and (c) on TPU substrates under stretching.

domain purity (~0.4), both before and after thermal annealing.[71,72] This consistency suggests that the PM6-DTzB10:Y6-BO blend preserved its initial morphology mainly due to enhanced P_D–SMA interaction and more strongly developed crystalline domains. Also, a similar trend was observed in their AFM height images. The root-mean-square averaged roughness (R_q) value of the PM6:Y6-BO blend increased from 1.3 to 1.9 nm after 24 h of heating. The increased R_q values and the formation of agglomerates on the PM6:Y6-BO blend are indicative of its unstable initial blend morphology. In contrast, the PM6-DTzB10:Y6-BO blend exhibited almost the same R_q value from 1.2 to 1.3 nm under identical heating conditions. These results confirm that the PM6-DTzB10:Y6-BO-based PSCs maintain their initial PSC performance under thermal stress by preserving their blend morphology.[73]

2.5. Mechanical properties

The mechanical robustness of the PSCs is a critical factor for their application as power suppliers in wearable devices.[74,75] At first, we evaluated the stretchability of neat P_D films using a pseudo free-standing tensile test (Fig. S15 and Table S8†).[76,77] Interestingly, both the COS value and toughness were enhanced with the incorporation of the DTzB unit into the P_D backbone. Specifically, the COS values increased in the following order: PM6 (16.9%) < PM6-DTzB5 (20.7%) < PM6-DTzB10 (23.1%) < PM6-DTzB20 (28.0%) films. This improvement in the mechanical properties in the PM6-DTzB P_D could be attributed to its random terpolymer structure and increased intermolecular interaction between P_Ds, compared to PM6 P_D.

Next, we compared the stretchability of the P_D:Y6-BO blend films (Fig. 5a and Table S9†). All active layers were spin-coated using the same process for device fabrication. Since the SMA molecules typically exhibit unconnected brittle domains due to their inherent rigid structure, it is important to dissipate mechanical stress to prevent crack propagation in the SMA domains and at the interfaces between the P_D and SMA domains.[78] For example, the PM6:Y6-BO exhibited a relatively low COS of only 1.7%. In contrast, well-intermixed P_D:SMA domains have advantages in enhancing the film stretchability.[23] With an increasing content of the DTzB unit, the COS value increased from 5.5% for PM6-DTzB5:Y6-BO, to 11.7% for PM6-DTzB10:Y6-BO, and 17.0% for PM6-DTzB20:Y6-BO. Similarly, the toughness values also increased in the order of 0.2 MJ m^{-3} for PM6:Y6-BO, 1.0 MJ m^{-3} for PM6-DTzB5:Y6-BO, 2.5 MJ m^{-3} for PM6-DTzB10:Y6-BO, and 3.7 MJ m^{-3} for PM6-DTzB20:Y6-BO. Fig. 5b shows the optical microscope (OM) images of the PM6:Y6-BO and PM6-DTzB10:Y6-BO blend films upon stretching during a tensile test. The PM6:Y6-BO blend showed distinct crack formation even at a small strain of 3%. In contrast, the PM6-DTzB10:Y6-BO blend displayed plastic deformation without any observable cracks at a strain of 10%. This improvement in mechanical properties of DTzB-incorporated P_D-based blends is mainly attributed to the presence of a larger fraction of intermixed P_D:SMA domains, which effectively dissipates mechanical stress and suppresses crack propagation. Especially, the PM6-DTzB10:Y6-BO blend and PM6-DTzB20:Y6-BO blend contained more intermixed blend domains than the PM6:Y6-BO blend, as shown in RSoXS profiles (Fig. 3c). These well-intermixed P_D:SMA blend domains can facilitate the dissipation of mechanical stress on the brittle Y6-BO domains and at fragile P_D:SMA interfaces.[23]

Additionally, the crack formation behavior while stretching the P_D:Y6-BO blend films on the thermoplastic polyurethane (TPU) substrate was compared to assess the potential of the DTzB-incorporated P_Ds in stretchable PSC applications (Fig. 5c).[79–81] For the PM6:Y6-BO blend, cracks were clearly observed at only 10% strain and rapidly propagated under 30% strain, despite the stress dissipation from the elastomer support. In contrast, the PM6-DTzB10:Y6-BO blend film did not show any visible cracks during stretching up to 30% strain.

3. Conclusions

We developed a series of PM6-DTzB terpolymers by introducing the planar structured DTzB unit into the PM6 P_D backbone and achieved efficient, thermally-stable, and mechanically robust PSCs by non-halogenated solvent processing. The introduction of an appropriate amount of the DTzB unit into the P_D backbone resulted in improved molecular compatibility with the Y6-BO SMA as well as enhanced crystalline and electrical transport abilities of the P_D film. This led to the formation of the blend morphology with sufficient P_D:SMA intermixed domains as well as well-developed crystalline domains of P_Ds and SMAs, enhancing both the charge generation and transport properties in the PSCs. Therefore, PM6-DTzB10:Y6-BO PSCs exhibited a higher PCE of 16.8% compared to that of PM6:Y6-BO PSCs (PCE = 15.6%) with solution processing in *o*-xylene. The optimized blend morphology of the PM6-DTzB10:Y6-BO was also beneficial in suppressing the burn-in degradation of PSCs while significantly improving the stretchability of the active layer. The PM6-DTzB10-based PSCs showed a higher thermal stability against annealing at 100 °C than the PM6-based PSCs. Moreover, the PM6-DTzB10:Y6-BO blend films demonstrated superior mechanical properties, exhibiting 7 times higher stretchability (COS = 11.7%) compared to the PM6-based blend (COS = 1.7%).

Author contributions

S. S and H. J. contributed equally to this work. S. S. and H. J. conceptualized this research, performed the investigation, and wrote the original draft. E. S. O., C. L., T. H-Q. N, and T. N-L. P. supported the investigation. J.-W. L, D. J, M. J. L, and T.-S. K. supported editing the draft. B. J. K. led data curation, project administration, funding acquisition, and editing the draft.

Conflicts of interest

The authors declare no conflict of interest.

Acknowledgements

This work was supported by the National Research Foundation of Korea (2020M3H4A1A02084906 and RS-2023-00283244). This

research used resources of the Advanced Light Source, which is a DOE Office of Science User Facility under contract no. DE-AC02-05CH11231.

References

1 K. Fukuda, K. Yu and T. Someya, *Adv. Energy Mater.*, 2020, **10**, 2000765.
2 E. Dauzon, X. Sallenave, C. Plesse, F. Goubard, A. Amassian and T. D. Anthopoulos, *Adv. Mater.*, 2021, **33**, 2101469.
3 C. Lee, S. Lee, G.-U. Kim, W. Lee and B. J. Kim, *Chem. Rev.*, 2019, **119**, 8028–8086.
4 X. Dong, Y. Jiang, L. Sun, F. Qin, X. Zhou, X. Lu, W. Wang and Y. Zhou, *Adv. Funct. Mater.*, 2022, **32**, 2110209.
5 Q. Liu, Y. Jiang, K. Jin, J. Qin, J. Xu, W. Li, J. Xiong, J. Liu, Z. Xiao, K. Sun, S. Yang, X. Zhang and L. Ding, *Sci. Bull.*, 2020, **65**, 272–275.
6 L. Zhu, M. Zhang, J. Xu, C. Li, J. Yan, G. Zhou, W. Zhong, T. Hao, J. Song, X. Xue, Z. Zhou, R. Zeng, H. Zhu, C.-C. Chen, R. C. I. MacKenzie, Y. Zou, J. Nelson, Y. Zhang, Y. Sun and F. Liu, *Nat. Mater.*, 2022, **21**, 656–663.
7 C. Han, J. Wang, S. Zhang, L. Chen, F. Bi, J. Wang, C. Yang, P. Wang, Y. Li and X. Bao, *Adv. Mater.*, 2023, **35**, 2208986.
8 W. Gao, F. Qi, Z. Peng, F. R. Lin, K. Jiang, C. Zhong, W. Kaminsky, Z. Guan, C.-S. Lee, T. J. Marks, H. Ade and A. K.-Y. Jen, *Adv. Mater.*, 2022, **34**, 2202089.
9 G. Zhang, H. Ning, H. Chen, Q. Jiang, J. Jiang, P. Han, L. Dang, M. Xu, M. Shao, F. He and Q. Wu, *Joule*, 2021, **5**, 931–944.
10 J. Yi, M. Pan, L. Chen, Y. Chen, I. C. Angunawela, S. Luo, T. Zhang, A. Zeng, J. Chen, Z. Qi, H. Yu, W. Liu, J. Y. L. Lai, H. K. Kim, X. Zhu, H. Ade, H. Lin and H. Yan, *Adv. Energy Mater.*, 2022, **12**, 2201850.
11 B. Pang, C. Liao, X. Xu, L. Yu, R. Li and Q. Peng, *Adv. Mater.*, 2023, **35**, 2300631.
12 H. Liang, H. Chen, P. Wang, Y. Zhu, Y. Zhang, W. Feng, K. Ma, Y. Lin, Z. Ma, G. Long, C. Li, B. Kan, Z. Yao, H. Zhang, X. Wan and Y. Chen, *Adv. Funct. Mater.*, 2023, **33**, 2301573.
13 X. Yang, B. Li, X. Zhang, S. Li, Q. Zhang, L. Yuan, D.-H. Ko, W. Ma and J. Yuan, *Adv. Mater.*, 2023, **35**, 2301604.
14 S. Dong, T. Jia, K. Zhang, J. Jing and F. Huang, *Joule*, 2020, **4**, 2004–2016.
15 Z. Zhong, S. Chen, J. Zhao, J. Xie, K. Zhang, T. Jia, C. Zhu, J. Jing, Y. Liang, L. Hong, S. Zhu, D. Ma and F. Huang, *Adv. Energy Mater.*, 2023, **13**, 2302273.
16 Z. U. Rehman, M. Haris, S. U. Ryu, M. Jahankhan, C. E. Song, H. K. Lee, S. K. Lee, W. S. Shin, T. Park and J.-C. Lee, *Adv. Sci.*, 2023, **10**, 2302376.
17 H. Xia, Y. Zhang, W. Deng, K. Liu, X. Xia, C.-J. Su, U. S. Jeng, M. Zhang, J. Huang, J. Huang, C. Yan, W.-Y. Wong, X. Lu, W. Zhu and G. Li, *Adv. Mater.*, 2022, **34**, 2107659.
18 H. Lu, G. Ran, Y. Liu, Z. Pei, W. Liu, Y. Liu, Z. Tang, W. Zhang and Z. Bo, *Adv. Funct. Mater.*, 2023, **33**, 2301866.
19 C. Wang, X. Ma, Y.-f. Shen, D. Deng, H. Zhang, T. Wang, J. Zhang, J. Li, R. Wang, L. Zhang, Q. Cheng, Z. Zhang, H. Zhou, C. Tian and Z. Wei, *Joule*, 2023, **7**, 2386–2401.
20 S. Kim, H. Choi, M. Lee, H. Jung, Y. Shin, S. Lee, K. Kim, M. H. Kim, K. Kwak and B. Kim, *Polymers*, 2023, **15**, 1354.
21 T. Dai, P. Lei, B. Zhang, A. Tang, Y. Geng, Q. Zeng and E. Zhou, *ACS Appl. Mater. Interfaces*, 2021, **13**, 21556–21564.
22 S. Lee, D. Jeong, C. Kim, C. Lee, H. Kang, H. Y. Woo and B. J. Kim, *ACS Nano*, 2020, **14**, 14493–14527.
23 J.-W. Lee, D. Jeong, D. J. Kim, T. N.-L. Phan, J. S. Park, T.-S. Kim and B. J. Kim, *Energy Environ. Sci.*, 2021, **14**, 4067–4076.
24 K. Zhou, J. Xin and W. Ma, *ACS Energy Lett.*, 2019, **4**, 447–455.
25 L. Ye, M. Gao and J. Hou, *Sci. China Chem.*, 2021, **64**, 1875–1887.
26 K. Wang, Y. Li and Y. Li, *Macromol. Rapid Commun.*, 2020, **41**, 1900437.
27 W. Yang, Z. Luo, R. Sun, J. Guo, T. Wang, Y. Wu, W. Wang, J. Guo, Q. Wu, M. Shi, H. Li, C. Yang and J. Min, *Nat. Commun.*, 2020, **11**, 1218.
28 B. Li, Q. Zhang, S. Li, X. Yang, F. Yang, Y. Kong, Y. Li, Z. Wu, W. Zhang, Q. Zhao, Y. Zhang, H. Young Woo, J. Yuan and W. Ma, *Chem. Eng. J.*, 2022, **438**, 135543.
29 J.-W. Lee, C. Sun, D. J. Kim, M. Y. Ha, D. Han, J. S. Park, C. Wang, W. B. Lee, S.-K. Kwon, T.-S. Kim, Y.-H. Kim and B. J. Kim, *ACS Nano*, 2021, **15**, 19970–19980.
30 E. Van Hemelrijck, P. Van Puyvelde, S. Velankar, C. W. Macosko and P. Moldenaers, *J. Rheol.*, 2004, **48**, 143–158.
31 Y.-A. Su, N. Maebayashi, H. Fujita, Y.-C. Lin, C.-I. Chen, W.-C. Chen, T. Michinobu, C.-C. Chueh and T. Higashihara, *ACS Appl. Mater. Interfaces*, 2020, **12**, 12083–12092.
32 L. Hong, H. Yao, Z. Wu, Y. Cui, T. Zhang, Y. Xu, R. Yu, Q. Liao, B. Gao, K. Xian, H. Y. Woo, Z. Ge and J. Hou, *Adv. Mater.*, 2019, **31**, 1903441.
33 J. Kim, M. Kyeong, J.-W. Ha, H. Ahn, J. Jung, S. Seo, T. N.-L. Phan, C. Lee, S. C. Yoon, B. J. Kim and S.-J. Ko, *J. Mater. Chem. A*, 2021, **9**, 27551–27559.
34 C. Lim, S. Lee, D. Han, C. Lee and B. J. Kim, *Macromolecules*, 2022, **55**, 10395–10404.
35 J.-W. Lee, C. Lim, S.-W. Lee, Y. Jeon, S. Lee, T.-S. Kim, J.-Y. Lee and B. J. Kim, *Adv. Energy Mater.*, 2022, **12**, 2202224.
36 H. Lu, H. Wang, G. Ran, S. Li, J. Zhang, Y. Liu, W. Zhang, X. Xu and Z. Bo, *Adv. Funct. Mater.*, 2022, **32**, 2203193.
37 J. Kim, G.-U. Kim, D. J. Kim, S. Lee, D. Jeong, S. Seo, S.-J. Ko, S. C. Yoon, T.-S. Kim and B. J. Kim, *J. Mater. Chem. A*, 2023, **11**, 4808–4817.
38 X. Jing, Y. Zhao, Q. Wang, X. Kang, T. Zhuang, X. Liu, X. Wang, L. Yu and M. Sun, *Polymer*, 2022, **254**, 125089.
39 H. Jung, G. Yu, J. Kim, H. Bae, M. Kim, K. Kim, B. Kim and Y. Lee, *Sol. RRL*, 2021, **5**, 2100513.
40 S. Chen, H. J. Cho, J. Lee, Y. Yang, Z.-G. Zhang, Y. Li and C. Yang, *Adv. Energy Mater.*, 2017, **7**, 1701125.
41 J. Wang, C. Han, F. Bi, D. Huang, Y. Wu, Y. Li, S. Wen, L. Han, C. Yang, X. Bao and J. Chu, *Energy Environ. Sci.*, 2021, **14**, 5968–5978.
42 J. Wang, C. Han, S. Wen, F. Bi, Z. Hu, Y. Li, C. Yang, X. Bao and J. Chu, *Energy Environ. Sci.*, 2023, **16**, 2327–2337.

43 J. Wang, C. Han, J. Han, F. Bi, X. Sun, S. Wen, C. Yang, C. Yang, X. Bao and J. Chu, *Adv. Energy Mater.*, 2022, **12**, 2201614.
44 J. Wu, G. Li, J. Fang, X. Guo, L. Zhu, B. Guo, Y. Wang, G. Zhang, L. Arunagiri, F. Liu, H. Yan, M. Zhang and Y. Li, *Nat. Commun.*, 2020, **11**, 4612.
45 X. Guo, Q. Fan, J. Wu, G. Li, Z. Peng, W. Su, J. Lin, L. Hou, Y. Qin, H. Ade, L. Ye, M. Zhang and Y. Li, *Angew. Chem., Int. Ed.*, 2021, **60**, 2322–2329.
46 T. Zhang, C. An, Y. Cui, J. Zhang, P. Bi, C. Yang, S. Zhang and J. Hou, *Adv. Mater.*, 2022, **34**, 2105803.
47 G. Conboy, R. G. D. Taylor, N. J. Findlay, A. L. Kanibolotsky, A. R. Inigo, S. S. Ghosh, B. Ebenhoch, L. Krishnan Jagadamma, G. K. V. V. Thalluri, M. T. Sajjad, I. D. W. Samuel and P. J. Skabara, *J. Mater. Chem. C*, 2017, **5**, 11927–11936.
48 L. Xu, W. Tao, M. Guan, X. Yang, M. Huang, H. Chen, J. Zhang, B. Zhao and S. Tan, *ACS Appl. Energy Mater.*, 2021, **4**, 11624–11633.
49 E. Ahmed, S. Subramaniyan, F. S. Kim, H. Xin and S. A. Jenekhe, *Macromolecules*, 2011, **44**, 7207–7219.
50 L. Zhou, L. Meng, J. Zhang, C. Zhu, S. Qin, I. Angunawela, Y. Wan, H. Ade and Y. Li, *Adv. Funct. Mater.*, 2022, **32**, 2109271.
51 L.-H. Chou, T. Mikie, M. Saito, C.-L. Liu and I. Osaka, *ACS Appl. Mater. Interfaces*, 2022, **14**, 14400–14409.
52 J. Rivnay, S. C. B. Mannsfeld, C. E. Miller, A. Salleo and M. F. Toney, *Chem. Rev.*, 2012, **112**, 5488–5519.
53 S. Seo, J. Kim, H. Kang, J.-W. Lee, S. Lee, G.-U. Kim and B. J. Kim, *Macromolecules*, 2021, **54**, 53–63.
54 J. Zhang, Q. Huang, K. Zhang, T. Jia, J. Jing, Y. Chen, Y. Li, Y. Chen, X. Lu, H. Wu, F. Huang and Y. Cao, *Energy Environ. Sci.*, 2022, **15**, 4561–4571.
55 M. Mohan, V. Nandal, S. Paramadam, K. P. Reddy, S. Ramkumar, S. Agarwal, C. S. Gopinath, P. R. Nair and M. A. G. Namboothiry, *J. Phys. Chem. C*, 2017, **121**, 5523–5530.
56 S. R. Cowan, A. Roy and A. J. Heeger, *Phys. Rev. B*, 2010, **82**, 245207.
57 H. D. Kim, Y. Horiuchi, S. Iwasaki, T. Fukuhara and H. Ohkita, *ACS Appl. Mater. Interfaces*, 2021, **13**, 39322–39330.
58 D. K. Tran, A. Robitaille, I. J. Hai, X. Ding, D. Kuzuhara, T. Koganezawa, Y.-C. Chiu, M. Leclerc and S. A. Jenekhe, *J. Mater. Chem. A*, 2020, **8**, 21070–21083.
59 Y. Cai, Y. Li, R. Wang, H. Wu, Z. Chen, J. Zhang, Z. Ma, X. Hao, Y. Zhao, C. Zhang, F. Huang and Y. Sun, *Adv. Mater.*, 2021, **33**, 2101733.
60 Z. Li, L. Ying, P. Zhu, W. Zhong, N. Li, F. Liu, F. Huang and Y. Cao, *Energy Environ. Sci.*, 2019, **12**, 157–163.
61 D. R. Kozub, K. Vakhshouri, S. V. Kesava, C. Wang, A. Hexemer and E. D. Gomez, *Chem. Commun.*, 2012, **48**, 5859–5861.
62 J.-W. Lee, C. Sun, C. Lee, Z. Tan, T. N.-L. Phan, H. Jeon, D. Jeong, S.-K. Kwon, Y.-H. Kim and B. J. Kim, *ACS Energy Lett.*, 2023, **8**, 1344–1353.
63 W. Wang, Q. Wu, R. Sun, J. Guo, Y. Wu, M. Shi, W. Yang, H. Li and J. Min, *Joule*, 2020, **4**, 1070–1086.
64 L. J. Richter, D. M. DeLongchamp and A. Amassian, *Chem. Rev.*, 2017, **117**, 6332–6366.
65 L. Zhang, X. Xu, B. Lin, H. Zhao, T. Li, J. Xin, Z. Bi, G. Qiu, S. Guo, K. Zhou, X. Zhan and W. Ma, *Adv. Mater.*, 2018, **30**, 1805041.
66 K.-H. Kim, H. Kang, H. J. Kim, P. S. Kim, S. C. Yoon and B. J. Kim, *Chem. Mater.*, 2012, **24**, 2373–2381.
67 N. Gasparini, M. Salvador, S. Strohm, T. Heumueller, I. Levchuk, A. Wadsworth, J. H. Bannock, J. C. de Mello, H.-J. Egelhaaf, D. Baran, I. McCulloch and C. J. Brabec, *Adv. Energy Mater.*, 2017, **7**, 1700770.
68 R. Ma, Q. Fan, T. A. Dela Peña, B. Wu, H. Liu, Q. Wu, Q. Wei, J. Wu, X. Lu, M. Li, W. Ma and G. Li, *Adv. Mater.*, 2023, **35**, 2212275.
69 L. Ye, B. A. Collins, X. Jiao, J. Zhao, H. Yan and H. Ade, *Adv. Energy Mater.*, 2018, **8**, 1703058.
70 J. Lee, J. W. Kim, S. A. Park, S. Y. Son, K. Choi, W. Lee, M. Kim, J. Y. Kim and T. Park, *Adv. Energy Mater.*, 2019, **9**, 1901829.
71 J.-W. Lee, C. Sun, T. N.-L. Phan, D. C. Lee, Z. Tan, H. Jeon, S. Cho, S.-K. Kwon, Y.-H. Kim and B. J. Kim, *Energy Environ. Sci.*, 2023, **16**, 3339–3349.
72 C. Zhang, J. Song, J. Xue, S. Wang, Z. Ge, Y. Man, W. Ma and Y. Sun, *Angew. Chem., Int. Ed.*, 2023, **62**, e202308595.
73 B. Li, X. Yang, S. Li and J. Yuan, *Energy Environ. Sci.*, 2023, **16**, 723–744.
74 J. S. Park, G.-U. Kim, S. Lee, J.-W. Lee, S. Li, J.-Y. Lee and B. J. Kim, *Adv. Mater.*, 2022, **34**, 2201623.
75 D. J. Lipomi, B. C.-K. Tee, M. Vosgueritchian and Z. Bao, *Adv. Mater.*, 2011, **23**, 1771–1775.
76 J.-H. Kim, A. Nizami, Y. Hwangbo, B. Jang, H.-J. Lee, C.-S. Woo, S. Hyun and T.-S. Kim, *Nat. Commun.*, 2013, **4**, 2520.
77 T. Kim, J.-H. Kim, T. E. Kang, C. Lee, H. Kang, M. Shin, C. Wang, B. Ma, U. Jeong, T.-S. Kim and B. J. Kim, *Nat. Commun.*, 2015, **6**, 8547.
78 Q. Fan, W. Su, S. Chen, W. Kim, X. Chen, B. Lee, T. Liu, U. A. Méndez-Romero, R. Ma, T. Yang, W. Zhuang, Y. Li, Y. Li, T.-S. Kim, L. Hou, C. Yang, H. Yan, D. Yu and E. Wang, *Joule*, 2020, **4**, 658–672.
79 Q. Wan, S. Seo, S.-W. Lee, J. Lee, H. Jeon, T.-S. Kim, B. J. Kim and B. C. Thompson, *J. Am. Chem. Soc.*, 2023, **145**, 11914–11920.
80 S. Seo, J.-W. Lee, D. J. Kim, D. Lee, T. N.-L. Phan, J. Park, Z. Tan, S. Cho, T.-S. Kim and B. J. Kim, *Adv. Mater.*, 2023, **35**, 2300230.
81 J.-W. Lee, S. Seo, S.-W. Lee, G.-U. Kim, S. Han, T. N.-L. Phan, S. Lee, S. Li, T.-S. Kim, J.-Y. Lee and B. J. Kim, *Adv. Mater.*, 2022, **34**, 2207544.